IEEE Access
Multidisciplinary | Rapid Review | Open Access Journal

Received 1 July 2022, accepted 19 July 2022, date of publication 25 July 2022, date of current version 28 July 2022.

Digital Object Identifier 10.1109/ACCESS.2022.3193379

RESEARCH ARTICLE

Transistor Laser Antenna: Electromagnetic Model in Transmit and Receive Modes

ARMAN AFSARI[1], (Member, IEEE), PAULO DE SOUZA[1], (Senior Member, IEEE), AMIN ABBOSH[2], (Fellow, IEEE), AND YAHYA RAHMAT-SAMII[3], (Life Fellow, IEEE)

[1]School of Information and Communication Technology, Griffith University, Gold Coast, QLD 4215, Australia
[2]School of Information Technology and Electrical Engineering, The University of Queensland, Brisbane, QLD 4072, Australia
[3]Department of Electrical and Computer Engineering, University of California at Los Angeles, Los Angeles, CA 90095, USA

Corresponding author: Arman Afsari (a.afsari@griffith.edu.au)

ABSTRACT Transistor laser can drive recent innovative technologies like optical antennas and rectennas. To this end, this semiconductor device requires an accurate electromagnetic model capable of determining the antenna characteristics like radiation pattern, directivity, gain, bandwidth, and polarization. Nonetheless, the current semiconductor models of transistor laser describe the absorption and emission of light mainly by simplified expressions and circuit models. These models usually overlook the actual physical geometry and full-wave light-emitting analysis of the device. In this article, a comprehensive computational electromagnetic modeling and characterization is presented for transistor laser. The existing semiconductor and electromagnetic equations are reorganized in a systematic fashion, coupled, and solved numerically to get the electromagnetic field components emitted or absorbed by the device. These fields determine the radiation pattern, directivity, gain, bandwidth, and polarization of transistor laser in transmit and receive modes. The equations involved in the above electromagnetic model are the Poisson and continuity equations incorporating radiative and non-radiative recombination rates, the vector magnetic potential equation interacting with the Hamiltonian operator of electrons in valance and conduction bands, the equation of the dielectric properties fluctuations of semiconductor layers, and the Poynting vector determining the power flow. The constructed model demonstrates agreement with the general performance of the device in experimental reports.

INDEX TERMS Antenna theory, cavity antenna, laser, optical antenna, rectenna, renewable energy, solar energy.

I. INTRODUCTION

Transistor laser is considered as one of the five most important inventions in the history of Physics. It can speed up communications, data transfer, and computing immensely. Since the invention of the device by the IEEE frontier fellows, Milton Feng and Nick Holonyak, transistor laser has demonstrated breakthrough applications in modern electronics [1]. Fig. 1 shows the general structure of the semiconductor device, adopted from [1]. Some of these modern applications are discussed hereafter.

The associate editor coordinating the review of this manuscript and approving it for publication was Debdeep Sarkar.

A. TRANSISTOR LASER AS OPTICAL ANTENNA

Vertical cavity transistor laser (VCTL) is a lightweight and high-power optical source, which can operate as an optical antenna. Excellent bandwidth of the optical communication link provided by VCTL can significantly increase the data transfer rate up to 40 Gb/s [1]. The unique features of conventional optical antennas were investigated in [2]–[4] and the references therein. Those investigations led to sophisticated designs and further studies on optical antennas for communications [5] and beamforming applications [6]–[8]. Furthermore, the characteristics of optical antennas in terms of circuit [9] or full-wave models [10] added extensive knowledge to the existing literature. Possible contribution of VCTL to improve the bandwidth and point-to-point secured communications is thus understood.

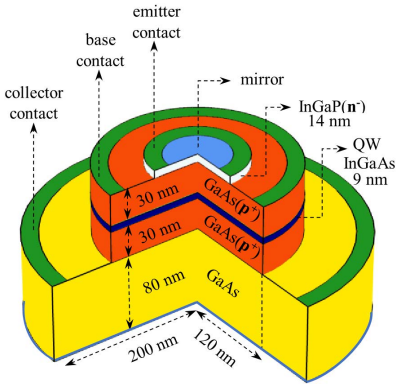

FIGURE 1. A typical VCTL with dimensions set for research purposes only (adopted from [1]). The optical transition leading to emission or absorption of light is mainly evaluated by the radiative recombination rates at quantum well (QW), overlooking the physics of electromagnetism across the device.

B. TRANSISTOR LASER AS OPTICAL RECTENNA

Global warming points to immediate and comprehensive research on renewable energies. As solar energy is the most sustainable energy to replace fossil fuels, special considerations are given to technologies capable of harvesting the sunlight. To convert sunlight into electricity, conventional solar cells are designed to rectify the full visible spectrum. Nevertheless, the maximum solar irradiance takes place at approximately 580 nm across the visible wavelength spectrum corresponding to the yellow light (inspiring the dimensions of Fig. 1) [11]. Optical rectifying antenna (rectenna) is a unique technology to absorb and rectify a specific visible wavelength [12]–[14].

Optical rectenna consists of a nanoscale antenna to absorb energy from a specific wavelength in visible spectrum, and a semiconductor device to rectify the absorbed light into direct current (DC) electricity [15]. The semiconductor device is typically a diode, and the antenna is usually considered as a small dipole connected to the diode, or a cavity embedded inside the diode [16]–[17]. The latter design features a by-product integration.

Regarding the unique features of VCTL, the device can be considered as a more appropriate candidate to operate as a rectenna. Foremost, the much faster switching capabilities of VCTL can provide a cleaner rectified signal when compared to diodes [1]. Having three terminals leads to easier cascaded integration on semiconductor wafers [1]. Because of the different transistor circuit topologies, matching to the harvester circuit can be realized optimally [18], [19]. Moreover, a larger amount of charge carriers in VCTL can potentially provide more rectified power in comparison with diodes [15].

C. TRANSISTOR LASER AS SOLAR SAIL

The hypothesis of interplanetary missions by spacecrafts propelled by solar sails has been under investigation since a long ago [20]. Yet, the major challenge of this propulsion system is the relatively heavy weight of the solar panels of every spacecraft compared to the minor force applied by solar photons to the solar sail. As the power of most of the current satellites and spacecrafts are provided by solar energy, large solar panels mounted on any satellite or spacecraft are currently one of the best technical approaches to supply the required power.

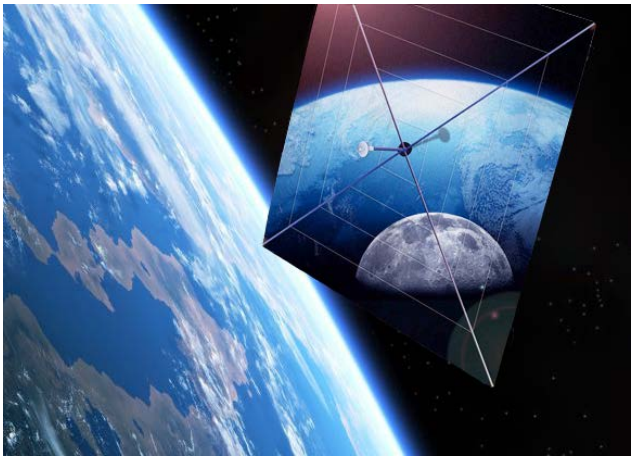

FIGURE 2. Hypothetical model of solar sail made of VCTL. Dimensions can be as small as the small satellites (cm to m). Precise polarization, radiation pattern, gain, and bandwidth of the device must be articulated by full-wave electromagnetic models.

The conclusion drawn in [21] is that the force applied by sunlight to the solar sail is as small as 10^{-5} N/m^2. Clearly, the remarkable weight of solar panels will significantly diminish the acceleration required for further motion in any spacecraft propelled by solar sail. Transistor lasers can, however, be manufactured on very thin and lightweight large wafers potentially functioning as solar sail and cell at the same time. As such, the outer surface of the VCTL in Fig. 1 (except the optical output/input) can be coated perfectly as a high-precision mirror to get the maximum propulsion from cosmic photons. This theoretical possibility will eliminate the need for additional solar panels as seen in Fig. 2.

D. EXISTING DC MODEL OF VCTL

Per Fig. 1 which is a typical replica of [1, Fig. 26], a VCTL consists of an intrinsic GaAs layer as collector. The two acceptor GaAs layers, that sandwich a quantum well (QW) made of InGaAs, form the base of the transistor, and a donor InGaP layer acts as emitter [1]. Two mirrors cover the top and bottom of the device to form an open vertical cavity distanced as an integer number of the operating wavelength of the VCTL. When the transistor is forward-biased, the extremely high recombination rate of the charge carriers in the QW leads to spontaneous and stimulated emission at the corresponding frequency [5].

If this physical mechanism is properly modeled in electromagnetics, VCTL in emission (transmit) mode can function as an optical antenna with given propagation, polarization, directivity, gain, efficiency, and bandwidth characteristics. In absorption (receive) mode, moreover, VCTL will function as an optical rectenna by characterizing the required photon density to turn the VCTL on. This attempt is considered as the motivation of this article, because the existing DC models of

VCTL discussed in Appendix I are based on some simplified steps to describe the device where the actual geometry of transistor laser is not taken into consideration.

E. PROPOSED DC MODEL FOR VCTL

Modeling nanoscale electromagnetic devices is a growing trend that has led to significant progress in developing optical antennas [22] and rectennas [23], [24]. Inspired by these recent works in [22]–[24], the Poisson equation which models the DC distribution of semiconductor quantities is coupled to the continuity equation containing extra radiative and non-radiative recombination rates in Section II. These rates, themselves, are constructed by a set of nonlinear semiconductor quantities reorganized in a systematic fashion. The entire radiative DC model is then coupled to the equation of vector magnetic potential representing the electromagnetic interactions with the electrons in the valance and conduction bands. During coupling, the dielectric properties of the device undergo minor fluctuations that need to be included in the model. When this flow of equations is nonlinearly coupled and computationally solved by any numerical method, say FEM-based electromagnetic solvers like COMSOL Multiphysics, a precise electromagnetic polarization and propagation pattern is achieved for VCTL. To the best of our knowledge, current models usually deal with VCTL from laser theory perspective, where scalar optical intensity is the only desired electromagnetic quantity. Section III verifies the proposed model implementing the VCTL in Fig. 1 in transmit (antenna) and receive (rectenna) modes. Finally, conclusions are drawn in Section IV.

II. VCTL MODEL IN ELECTROMAGNETICS

Usual electromagnetic semiconductor device modeling consists of two steps: the DC model, which initiates and biases the device, and the alternating current (AC) model (either in small or large signal regime) that studies the electromagnetic performance of the device. Light-emitting process of semiconductors, however, is a special mechanism wherein a DC bias leads to radiative electromagnetic fields in the form of light, in absence of any AC signal. As such, special theoretical considerations must be given to this aspect of electromagnetic radiation, particularly because any extra AC signal is then modulated by the light generated during DC bias. To build the proposed model, we are inspired by [25] and the references therein for initiation and bias, bring together the light-emitting equations discussed in [26]–[28], and incorporate an appropriate electromagnetic model from [29], [30].

A. INITIATION AND BIAS

The DC electric potential (V_{DC}) across the VCTL is governed by Poisson equation as [25],

$$\begin{aligned}\vec{\nabla}\cdot(\varepsilon_0\varepsilon_r\vec{\nabla}V_{DC}^{-}) &= q\underbrace{(n_0+N_n)}_{n}\\ \vec{\nabla}\cdot(\varepsilon_0\varepsilon_r\vec{\nabla}V_{DC}^{+}) &= -q\underbrace{(p_0+N_p)}_{p}\end{aligned} \tag{1a}$$

supported by the following boundary conditions,

$$\begin{aligned}V_{DC}^{base} = 0.8(V),\ V_{DC}^{emitter} = 0,\ V_{DC}^{collector} &= 1.5(V)\\ \hat{\boldsymbol{n}}_1\times(\vec{\nabla}V_{DC}) = 0, \quad &on\ mirrors\\ \hat{\boldsymbol{n}}_2\cdot(\varepsilon_0\varepsilon_r\vec{\nabla}V_{DC}) = 0, \quad &elsewhere\\ \hat{\boldsymbol{n}}_2\cdot\vec{\boldsymbol{J}}_{DC} = 0, \quad &elsewhere\end{aligned} \tag{1b}$$

where q is the charge of electron. The electron and hole densities n, p are determined by the corresponding intrinsic and doping amounts i.e., n_0, p_0 and N_n, N_p across the entire VCTL. Moreover, $\vec{\nabla}$ is the gradient operator (arrow sign is used to show vectors in space coordinates) and $\varepsilon_0, \varepsilon_r$ are the free-space and relative permittivity, respectively. Poisson equation in (1) is supported by the Dirichlet boundary condition (in Volts) on the terminal contacts of Fig. 1 where bias voltages are defined explicitly (values shown are typical). The Neumann insulation boundary condition is defined on the surrounding boundaries of the device with outward normal unit vector $\hat{\boldsymbol{n}}_2$, except the top and bottom mirrors with outward normal unit vector $\hat{\boldsymbol{n}}_1$ where perfect electric conductor boundary condition will support the Poisson equation. The continuity boundary condition of finite element method is naturally satisfied on the interface between semiconductor layers. Superscripts "+" and "-" stand for the positive and negative charges [25].

To determine the DC performance of the device completely, DC potential is then coupled to the flow of DC current, governed by the continuity equation across the device. Charge conservation for current density $\vec{\boldsymbol{J}}_{DC}$ suggests,

$$\begin{aligned}\vec{\nabla}\cdot\vec{\boldsymbol{J}}_{DC}^{-} &= 0\\ \vec{\nabla}\cdot\vec{\boldsymbol{J}}_{DC}^{+} &= 0\end{aligned} \tag{2}$$

where per [25],

$$\begin{aligned}\vec{\boldsymbol{J}}_{DC}^{-} &= qn\mu_n\vec{\nabla}E_c + \mu_n K_B T\vec{\nabla}n\\ \vec{\boldsymbol{J}}_{DC}^{+} &= qp\mu_p\vec{\nabla}E_v - \mu_p K_B T\vec{\nabla}p\end{aligned} \tag{3}$$

with K_B, T, μ as the Boltzmann constant, temperature, and carrier mobility, respectively. The thermal equilibrium conduction and valence band energies E_c, E_v are defined as,

$$\begin{aligned}E_c &= -(V_{DC}+\xi_0)\\ E_v &= -(V_{DC}+\xi_0+E_g)\end{aligned} \tag{4}$$

In (4), E_g and ξ_0 are the bandgap energy and electron affinity, respectively. Through a straightforward FEM iterative computational process, equations (1) and (2) are coupled and solved to derive the initial distributions of V_{DC}, n, p. Typical semiconductor quantities used in this paper are given in Table 1, inspired by [1] and [25]. We assume that the device is maintained in constant temperature, excluding the impact of thermal lensing [31] appearing as an extra term $\vec{\nabla}T$ in (3).

B. CARRIER RECOMBINATION IN VCTL

During light emission, two types of electron-hole recombination rates must be included in the VCTL model through

TABLE 1. Semiconductor properties of VCTL.

Parameter	Description	InGaAs	GaAs	InGaP
m_e	Electron effective mass	0.041	0.067	0.088
m_h	Hole effective mass	0.45	0.47	0.70
E_g	Bandgap energy (eV)	0.75	1.42	1.79
ξ_0	Electron affinity (eV)	4.50	4.07	4.10
μ_n, μ_p	Carrier mobility	10^4, 10^2	10^4, 10^2	10^4, 10^2
n_c	Conduction band effective density of states (cm^{-3})	2.1×10^{17}	8.6×10^{13}	9.7×10^{17}
N^- & N^+	Doping (cm^{-3})	Intrinsic	Intrinsic for collector 10^{18} for base	10^{17}
n_v	Valence band effective density of states (cm^{-3})	7.7×10^{18}	1.8×10^{15}	2.1×10^{19}
t_{spon}	Recombination lifetime (ps)	29	132	120
ε_{r_0}	Relative permittivity (initial)	13.9	12.9	11.8
σ_0	Conductivity (initial) (S/m)	0.1008	0.0000002 for collector 256000 for base	900000

The values are chosen for research purposes only and do not refer to any specific applications. They are, however, within the usual range of semiconductor device parameters for VCTL [26]-[30]. Optical angular frequency is $\omega_0 = 2\pi\times517\ (\mathrm{THz})$.

the charge conservation relation (2) [26, Ch. 6]: The spontaneous and stimulated "radiative" (optical) recombination rates (R_{rad}^{spon}, R_{rad}^{stim}) and the "non-radiative" Auger recombination rate (R_{Au}). The latter is merely applicable to semiconductors with high level of doping like VCTL, to consider the ionization effects of charge carriers [26]. During absorption of light, the similar but reverse mechanism is called carrier generation.

The above recombination processes will update the DC continuity equations as,

$$\begin{aligned}\vec{\nabla}\cdot\vec{J}_{DC}^{-} &= q(R_{Au}+R_{rad}^{spon}+R_{rad}^{stim})\\ \vec{\nabla}\cdot\vec{J}_{DC}^{+} &= -q(R_{Au}+R_{rad}^{spon}+R_{rad}^{stim})\end{aligned} \tag{5}$$

where the recombination rates are defined as [26],

$$\begin{aligned}R_{Au} &= C(n^2p+p^2n)\\ R_{rad}^{spon} &= \alpha np\\ R_{rad}^{stim} &= -\frac{2\pi}{\hbar}\mathrm{I}^2\,(f_v-f_c)\,g\end{aligned} \tag{6}$$

with the Auger recombination factor $C \sim 10^{-31}\left(1/cm^6s\right)$ and radiative capture probability $\alpha \sim 10^{-11}\left(1/cm^3s\right)$ [26]. While R_{Au} and R_{rad}^{spon} are directly evaluated by the basic semiconductor quantities, the stimulated recombination rate R_{rad}^{stim} requires special considerations and quantities that are discussed hereafter.

The quantities $\hbar, \mathrm{I}, f_v, f_c, g$ are respectively the reduced Plank's constant, matrix element, quasi-Fermi distributions of charge carriers in the valence and conduction bands, and the reduced density of photon states [25]–[28]. The quasi-Fermi distributions of charge carriers in the valence and conduction bands are described as [27],

$$f_v = \frac{1}{1+e^{\frac{E_{fp}-E_{1v}}{K_BT}}},\quad f_c = \frac{1}{1+e^{\frac{E_{2c}-E_{fn}}{K_BT}}} \tag{7}$$

where E_{2c}, E_{1v} stand for the conduction and valence band energies in thermal non-equilibrium defined as,

$$\begin{aligned}E_{2c} &= E_c+\frac{m_r}{m_e}(\hbar\omega_0-E_g)\\ E_{1v} &= E_v-\frac{m_r}{m_h}(\hbar\omega_0-E_g)\end{aligned} \tag{8}$$

with the joint effective mass of electrons (e) and holes (h) as $m_r^{-1} = m_e^{-1}+m_h^{-1}$ given in Table 1. Moreover, E_{fn}, E_{fp} denote the quasi-Fermi energy of electrons and holes as [25],

$$\begin{aligned}E_{fn} &\approx E_c - K_BT\ln(\frac{n_c}{N_n})\\ E_{fp} &\approx E_v + K_BT\ln(\frac{n_v}{N_p})\end{aligned} \tag{9}$$

where n_c, n_v are the effective density of states in conduction and valence bands, respectively, given in Table 1. Finally, the reduced density of photon states g is determined by [28],

$$g = \frac{1}{2\pi^2}\left(\frac{2}{\hbar^2}m_r\right)^{\frac{3}{2}}\sqrt{\hbar\omega_0-E_g} \tag{10}$$

with ω_0 as the angular frequency of light.

C. ELECTROMAGNETIC INTERACTION AND MATRIX ELEMENT

In electromagnetics, VCTL is considered as an open cavity wherein the coherent photons ($\vec{A}$) stimulate each other, say in the fundamental mode TEM_{00} [31]. This stimulation for each charge carrier is regarded as an external electromagnetic field that perturbs the ground state of the charge carrier [29], [30]. The effect of stimulating photons is described by the eigenvalue equation of the magnetic potential across the VCTL cavity as [32],

$$\vec{\nabla}\times\vec{\nabla}\times\vec{A}-\omega_0^2\mu_0\varepsilon_0\left(\varepsilon_r-j\frac{\sigma}{\omega_0\varepsilon_0}\right)\vec{A}=0$$

$$\hat{\boldsymbol{n}}_1 \times \vec{\boldsymbol{A}} = 0$$
$$\hat{\boldsymbol{n}}_2 \times \left(\vec{\nabla} \times \vec{\boldsymbol{A}}\right) + j\omega_0 \sqrt{\mu_0 \varepsilon_0 \left(\varepsilon_r - j\frac{\sigma}{\omega_0 \varepsilon_0}\right)} \times \left(\left(\hat{\boldsymbol{n}}_2 \cdot \vec{\boldsymbol{A}}\right)\hat{\boldsymbol{n}}_2 - \vec{\boldsymbol{A}}\right) = 0 \quad (11)$$

with μ_0 as free-space permeability, and σ as conductivity of each semiconductor layer, respectively. Moreover, $j = \sqrt{-1}$. The perfect electric conductor boundary condition is applied on the mirrors and contacts of VCTL in Fig. 1 with unit normal vector $\hat{\boldsymbol{n}}_1$, while the impedance boundary condition is applied to the rest of the surrounding boundaries with unit normal vector $\hat{\boldsymbol{n}}_2$. The eigenvalue problem in (11) is sometimes expressed by replacing ω_0^2 and $(\omega^2 - \omega_0^2)$ if higher-order cavity modes are of special interest. Following this, the interaction between $\vec{\boldsymbol{A}}$ and semiconductor quantities is investigated to construct the electromagnetic model of the device. It is noted that in conventional antenna engineering literature, antenna characteristics are derived directly by solving the vector electric field equation. However, the interaction between electromagnetics and semiconductor quantities is through the Hamiltonian operator, which is described by the magnetic potential not the electric field [28].

The ground state (valance band) of a charge carrier can be expressed by the Schrodinger equation as [29], [30],

$$\mathrm{H}_v \Psi_v = E_v \Psi_v \quad (12)$$

where Ψ_v is the wavefunction of a charge carrier at ground state. The stationary Hamiltonian is given as,

$$\mathrm{H}_v = \frac{1}{2m}\left(-j\hbar\vec{\nabla}\right)^2 + qV_{DC} \quad (13)$$

with m as the mass of the charge carrier.

For each photon described by $\vec{\boldsymbol{A}}$ to perturb the state of the charge carrier and energize it to the conduction band, the stationary Hamiltonian must be updated as [28],

$$\mathrm{H}_c = \frac{1}{2m}\left(-j\hbar\vec{\nabla} - q\vec{\boldsymbol{A}}\right)^2 + qV_{DC} \quad (14)$$

The above interaction between a photon and a charge carrier is, in general, a nonlinear process referred to as the nonlinear optical interaction. However, the updated Hamiltonian can be simplified in many practical applications to consider the perturbation as a linear action without a remarkable loss of accuracy [28].

To this end, we first implement the Coulomb gauge $\vec{\nabla} \cdot \vec{\boldsymbol{A}} = 0$ in (14) preferred to simplify the above equations [32], with respect to some more complicated trials on implementing the Lorenz gauge [33]. This gauge ensures that the DC and AC models are dealt with separately [25]. Second, we note that the nonlinear term $q^2\vec{\boldsymbol{A}} \cdot \vec{\boldsymbol{A}}$ is usually much smaller than $\hbar^2\vec{\nabla} \cdot \vec{\nabla}$ when acting on the wavefunction in many practical applications [27], [28]. Hence, ignoring the interaction of photon by itself i.e., $\vec{\boldsymbol{A}} \cdot \vec{\boldsymbol{A}}$ will not noticeably affect the accuracy of the device model, while maintaining the device model in the linear optics regime. Therefore,

$$\mathrm{H}_c \approx \mathrm{H}_v + \tilde{\mathrm{H}}$$

$$\tilde{\mathrm{H}} = \frac{q}{2m}\left(-j\hbar\vec{\boldsymbol{A}} \cdot \vec{\nabla}\right) \quad (15)$$

which leads to the excited state of charge carriers Ψ_c at conduction band as,

$$\mathrm{H}_c \Psi_c = E_c \Psi_c \quad (16)$$

As seen, the perturbation $\tilde{\mathrm{H}}$ stands for the energy difference between the ground and excited states as $E_c - E_v = E_g$.

D. TRANSLATION TO MACROSCOPIC DOMAIN

The interaction between the classical macroscopic quantity $\vec{\boldsymbol{A}}$ and the quantum quantity $-j\hbar\vec{\nabla}$ must appropriately be articulated. In many practical situations, the wavelength of the interacting photon $\vec{\boldsymbol{A}}$ is drastically larger than the microscopic domain occupied by an electron across which $-j\hbar\vec{\nabla}$ is applied. Therefore, we can apply a legitimate assumption called dipole approximation by disregarding the extremely slowly-varying phase of $\vec{\boldsymbol{A}}$ during interactions [28, Ch. 9].

Following this, we need to determine the matrix element I of VCTL in (6) which is critical to couple the microscopic and macroscopic quantities [28]. To this end, both the ground and excited state wavefunctions are expanded by Bloch orthogonal basis functions as [28, Ch. 9],

$$\Psi_v = u_v e^{jk_v \cdot r}$$
$$\Psi_c = u_c e^{jk_c \cdot r} \quad (17)$$

with u, k, r as a periodic function, crystal momentum, and radial coordinate, respectively. The transition coefficient (or matrix element) I between the two states is thus derived by Fermi's golden rule as,

$$\begin{aligned}
\mathrm{I} &= \int \Psi_c^* \tilde{\mathrm{H}} \Psi_v \, d\Lambda \\
&\approx \frac{q}{2m}|\vec{\boldsymbol{A}}| \cdot \int u_c^* e^{-jk_c \cdot r}\left(-j\hbar\vec{\nabla}\right) u_v e^{jk_v \cdot r} \, d\Lambda \\
&\approx \frac{q}{2m}|\vec{\boldsymbol{A}}| \cdot e^{-j(k_c - k_v)\cdot r} \int u_c^* \left(-j\hbar\vec{\nabla} u_v\right) d\Lambda \\
&\quad + \frac{q}{2m}|\vec{\boldsymbol{A}}| \cdot \int u_c^* u_v e^{-jk_c \cdot r}\left(-j\hbar \underbrace{\vec{\nabla} e^{jk_v \cdot r}}_{\approx 0}\right) d\Lambda
\end{aligned} \quad (18a)$$

where the slowly varying feature of the exponential term has been applied to the last two integrals via dipole approximation. More precisely, the wavelength of the photon in Fig. 1 is approximately 580 nm. This length is drastically larger than the dimensions occupied by an electron (Λ) during transition. Hence, for an electron transition from valence to conduction band or vice versa, the spatial variations of the magnetic vector potential can be neglected. This means that $|\vec{\boldsymbol{A}}|$ can be dealt with as a constant with respect to the differential of the integral operator i.e. $d\Lambda$, and the variations of the wavenumber k_c, k_v can be considered negligible.

Applying some features of the basis functions in (17) can further simplify (18a). Apparently, I vanishes due to orthogonality unless for a direct bandgap transition $k_c = k_v$. This

involves a Dirac delta function $\delta_{k_c k_v}$ in the calculation of (18a) [28, Fig. 9.2]. Therefore,

$$\mathrm{I} \approx \frac{q}{2m}|\vec{A}| \cdot \int u_c^* \left(-j\hbar\vec{\nabla} u_v\right) \delta_{k_c k_v} d\Lambda \tag{18b}$$

The above derivation of matrix element is accurate from theoretical perspective, giving a clear linear relation between the magnetic vector potential and the matrix element. Nonetheless, the calculation of the above integral in rather difficult in practice, as a precise form of Bloch functions is required to model each transition state. In addition, to calculate the total stimulated emission we have to sum (18b) over all the unit cells of VCTL which is not a practical trial.

An alternative approach is, however, to get a closed form equation for the matrix element using an analogy in calculating the probability of transition between the conduction and valence bands. This analogy is taken from the momentum conservation relation as reported by [28],

$$\mathrm{W} = \frac{2\pi}{\hbar}|\mathrm{I}|^2 \delta_{k_c k_v} \tag{18c}$$

and the same probability from thermodynamic considerations as [28],

$$\mathrm{W} = \left(\frac{\pi^2 c^3 \varepsilon_0 \varepsilon_r}{2\gamma^3 \omega_0 t_{spon}}\right) |\vec{A}|^2 \delta_{k_c k_v} \tag{18d}$$

Equating the above relations leads to,

$$\mathrm{I} \approx \left(\frac{\hbar\pi c^3 \varepsilon_0 \varepsilon_r}{4\gamma^3 \omega_0 t_{spon}}\right)^{\frac{1}{2}} |\vec{A}| \tag{19}$$

where t_{spon} is the spontaneous recombination lifetime given in Table 1, and γ is the real part of the refractive index as [32],

$$\gamma = \sqrt{\frac{|\varepsilon_r - j\frac{\sigma}{\omega_0 \varepsilon_0}| + \varepsilon_r}{2}} \tag{20}$$

As seen, the entire procedure from (12) to (18) was some intermediate manipulation to get (19), that we incorporate into the electromagnetic model. Detailed discussions on the above equations are given in [28, Ch. 9].

The last step of developing the electromagnetic model of VCTL is to consider the variation of the dielectric properties of VCTL layers in electromagnetic interactions. During light emission or absorption, the dielectric properties of different layers of VCTL slightly fluctuate around their initial values (indicated by subscript "i") as,

$$\begin{aligned} \sigma &\approx \sigma_i + \frac{4\pi}{\omega_0 |\vec{A}|^2} \mathrm{I}^2 (f_v - f_c)\, g \\ \varepsilon_r &\approx \varepsilon_{r_i} + \frac{8}{\omega_0 \varepsilon_0 |\vec{A}|^2} \mathrm{I}^2 g \int_{BW} \frac{(f_v - f_c)\,\omega}{\omega^2 - \omega_0^2} d\omega \end{aligned} \tag{21}$$

As the laser bandwidth (BW) usually occupies a small portion of spectrum around the central frequency ω_0, the integral in (14) will have a very small value and the corresponding change in the real part of the relative permittivity may be negligible. The computational coupling flowchart in Fig. 3 summarizes the proposed model solved iteratively by FEM until the computational error in (1), (5), and (11) becomes negligible. The exchange of variables in Fig. 3 shows how the laser quantities in the proposed electromagnetic model are updated at each iteration. The circuit model of VCTL is also embedded in Fig. 3 to insist that VCTL differs from conventional transistors in an extra optical port.

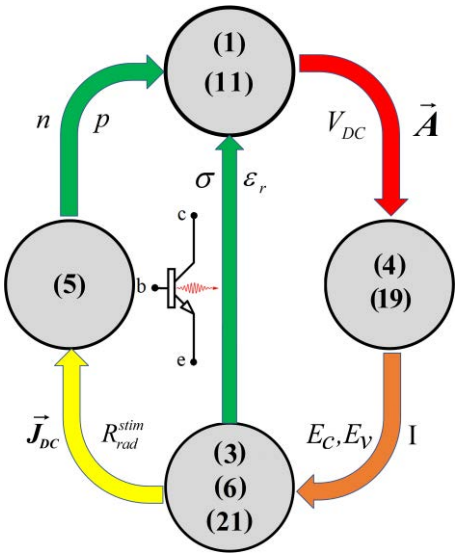

FIGURE 3. Computational coupling of the equations involved in the proposed electromagnetic model of VCTL, containing the conventional circuit model of the device as well.

E. DERIVATION OF CLASSICAL FIELDS

Upon solving the proposed computational flowchart in Fig. 3, the optical electric and magnetic fields emitted by VCTL are accordingly determined over the top mirror of VCTL as [32],

$$\begin{aligned} \vec{E} &= \beta\left(-j\omega_0 \vec{A}\right) \\ \vec{H} &= \beta\left(\frac{1}{\mu_0}\vec{\nabla} \times \vec{A}\right) \end{aligned} \tag{22}$$

with $\beta \approx 0.01$ as the imperfect coating coefficient of the top mirror. Depending on the application, β determines the magnitude of electromagnetic fields propagating outside the laser. The electromagnetic radiation by VCTL in the next section is thus shown qualitatively, as less significance can be attributed to the value of β. Following (22), the normalized optical output power is evaluated by the Poynting vector $|\vec{E} \times \vec{H}|$. It is noted that formulating the problem by Coulomb gauge $\vec{\nabla} \cdot \vec{A} = 0$ does not recognize or involve the electromagnetic scalar potential in the calculations.

The aforementioned electromagnetic fields derived by the proposed DC model can be regarded as a carrier signal appropriate to modulate an envelope, for instance. The modulation of a small or large AC envelope in the proposed VCTL model, with frequency ω_{AC}, can straightforwardly be considered in (1) and (5) as:

$$V_{DC}^{base} = 0.8 + V_{AC}(V)$$

$$\vec{\nabla}\cdot\vec{J}_{DC}^{-} = q(R_{Au} + R_{rad}^{spon} + R_{rad}^{stim} + j\omega_{AC}n)$$
$$\vec{\nabla}\cdot\vec{J}_{DC}^{+} = -q(R_{Au} + R_{rad}^{spon} + R_{rad}^{stim} + j\omega_{AC}p) \quad (23)$$

which is essentially equal to the conventional AC models of transistors discussed in details in [25]. The above derivation is then implemented for S-parameter analysis of the device when used as an antenna.

III. VCTL AS ANTENNA AND RECTENNA

In this section, the proposed model for VCTL is implemented firstly to evaluate the emission of light. The absorption procedure is then studied to evaluate the induced potential and current across the device. The presented figures are sometimes on logarithmic scales, as their linear scales have extremely large values. Agreement with experimental reports is then referenced accordingly. All the equations are constructed in the Partial Differential Equation Module of COMSOL Multiphysics which is a FEM-based solver.

A. VCTL AS OPTICAL ANTENNA

Fig. 4 shows the electromagnetic emission of light by VCTL. In Fig. 4(a), the most critical factor of light emission i.e., the emission rate is depicted across the device. As seen, the QW has significant contribution in the emission of light across the VCTL. The contour of the magnetic power is also shown qualitatively.

Electron and hole concentrations are also depicted across the semiconductor layers in Figs. 4(b) and 4(c) where the concentration of electrons repels the holes, mainly in the vicinity of QW. In Figs. 4(b) and 4(c), the electric power and magnetic field polarization derived by (22) are also shown qualitatively. The other important semiconductor quantity is the total recombination rate, which is shown in Fig. 4(d), followed by the electric field polarization. The recombination rate is extremely high inside the QW due to the very short recombination time [28].

The full magnetic and electric fields in Figs. 4(c) and 4(d) show a clock-wise (right-handed) circular polarization pattern propagating from near-field to far-field. In cylindrical coordinates, the electric field oscillates alongside the radial axis in Fig. 4(c), while the magnetic field oscillates alongside the angular coordinate in Fig. 4(d). Since the fields are perpendicular and the laser cavity is open, the above polarization mode (state) corresponds to TEM_{00}, which is regarded as the fundamental mode of open-cavity lasers.

B. VCTL AS OPTICAL RECTENNA

Following the transmit mode, the performance of VCTL in receiving mode is studied. During the absorption of light, the DC potential and current induced in the VCTL can be used for energy harvesting. The induced voltage can turn on the transistor when reaching the base-emitter forward-bias voltage.

Figs. 5(a) and 5(b) show the same VCTL of the previous subsection in the receive mode, illuminated by a surrounding plane wave at the same operating frequency of VCTL that is ω_0. The figures are on transparent mode to clearly visualize the distribution of induced quantities across the device.

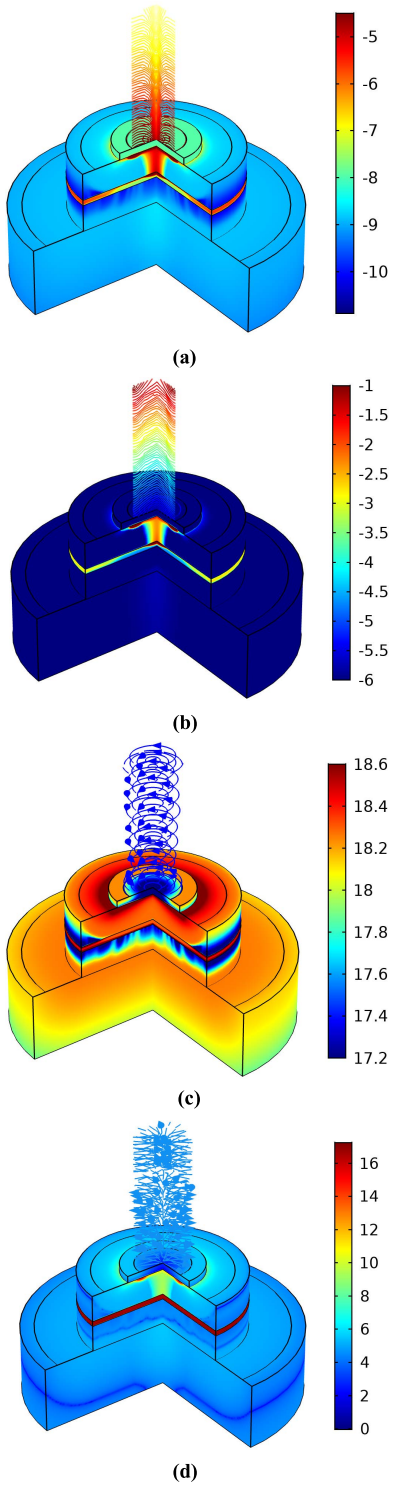

FIGURE 4. As a laser antenna, the proposed model of VCTL supports propagation, power flow, and polarization patterns of light. (a) Emission rate (log) (W/m^3) and the contour of magnetic power. (b) Electron concentration (log) ($1/m^3$) and the contour of electric power. (c) Hole concentration (log) ($1/m^3$) and the streamlines of magnetic fields. (d) Recombination rate (log) ($1/m^3s$) and the streamlines of electric fields.

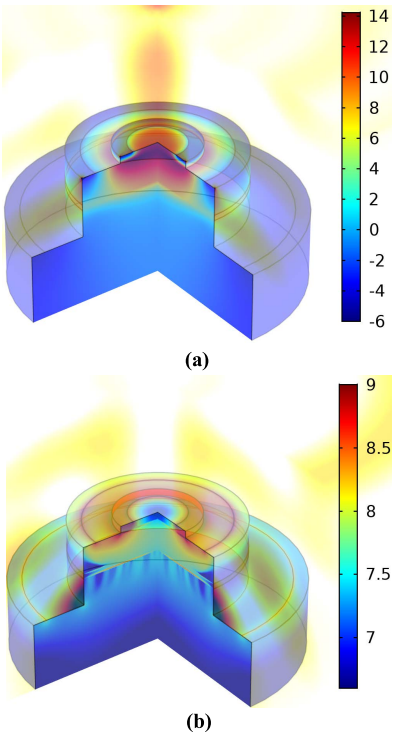

FIGURE 5. As a rectenna, the proposed device model of VCTL supports the absorption of light and the corresponding induced voltage (V) and current density (A/m^2) in (a) and (b), respectively.

Fig. 5(a) demonstrates how the induced electric potential can reach the desired base-emitter voltage to turn on the transistor. The distribution of the induced DC potential across the device shows the capability of VCTL to harvest and rectify the sunlight power. The norm of the electric field resembling the solar irradiance surrounding the device is also shown qualitatively. As such, Fig. 5(b) shows the induced current density across the VCTL with huge flow around the base-emitter region. The norm of the magnetic plane wave surrounding the device is also shown in a qualitative manner.

C. AGREEMENT WITH EXPERIMENTS

The proposed device model for VCTL, when undergoing a parametric sweep on different semiconductor quantities, shows adequate agreement with the general trend of experimental reports in [1] and circuit analysis in [34]. In particular, the variation of the normalized optical output power is evaluated by sweeping the two critical bias quantities of VCTL i.e., the base current (I_B) and the collector-emitter (V_{CE}) voltage. It is worth mentioning that the output power corresponds to the S-parameter $|S_{31}|$ defined as [35],

$$\begin{aligned} S_{31} &= \beta' \frac{4\pi}{c} \int_{\vec{s}} \left(\vec{E}_3 \times \vec{H}_1 - \vec{E}_1 \times \vec{H}_3 \right) \cdot d\vec{s} \\ &= 4\pi\beta'\beta^2 \frac{j\omega_0}{\mu_0 c} \int_{\vec{s}} \left(\left(\vec{A}_1 \right) \times \left(\vec{\nabla} \times \vec{A}_3 \right) - \left(\vec{A}_3 \right) \right. \\ &\quad \left. \times \left(\vec{\nabla} \times \vec{A}_1 \right) \right) \cdot d\vec{s} \end{aligned} \tag{24}$$

where β' is a calibration constant and c is the light velocity. As the normalized output power is more indicative, we omit the coefficient $4\pi\beta'\beta^2 j\omega_0/\mu_0 c$ during normalization. The above integral is taken over the surface of the upper mirror i.e., $\vec{s}$. To describe (24) in terms of the absolute optical output power at port 3 $|P_3|$, we merely need to multiply $|S_{31}|^2$ by the electric input power at port 1 $|P_1| = |V_B(V) I_B\ (mA)|$ i.e.,

$$|P_3| = |P_1|\,|S_{31}|^2 \tag{25}$$

It is noted, however, that the above definition of input power is a representative definition only, and may be redefined per different applications. In Fig. 6(a), the optical output power shows a sharp increase by increasing the driving current I_B for three different V_{CE} values. These values of V_{CE} were chosen per the lower, upper, and middle points of the active region of VCTL. As seen, increasing I_B leads to the saturation region. In Fig. 6(b), the effect of the collector bias voltage is studied on the optical output power. Increasing the V_{CE} for moderate values of I_B (relative to the small dimensions of the device in Fig. 1) demonstrates a linear trend with respect to the rise of the optical output power before entering the saturation; the trend that is roughly similar to diodes. For larger values of I_B, however, the trend is more nonlinear with respect to diodes, since the minority carrier electrons primarily occupy the quantum states of QW. As such, while in diode lasers the charge densities are mainly bounded at and beyond the threshold, this is not essentially true for VCTL [1, Fig. 10]. As the dielectric fluctuations in (21) slightly affect $\vec{A}$ in (11), some fluctuations are observed in optical response figures.

Following the above DC analysis, the small signal analysis of the developed model is also studied at microwave frequencies in Fig. 6(c) where $V_{CE} = 3$ V. In a common-emitter configuration discussed in (1), the base-emitter junction is regarded as the first port, the collector-emitter junction as the second port, and the optical port (upper mirror) as the third port representing the subscript numbers in (24). Fig. 6(c) shows that VCTL can modulate the microwave signal stably across a wide frequency band. Nevertheless, the optical output gradually reduces at upper microwave frequencies. This is because ω_{AC} is no longer negligible with respect to ω_0, which disturbs the cavity resonance frequency from ω_0 to $\omega_0 \pm \omega_{AC}$. In time domain, this is identical to partially disturbing t_{spon}. As such, if the VCTL in Fig. 1 is biased with $I_B = 9$ mA and $V_{CE} = 3$ V as typical values, ω_{AC} must be below 0.7 GHz to be modulated properly. This is of special interest in many applications like antenna arrays, where the amplitude and phase of each array element dynamically changes during agile adaptive beamforming [36]. Other frequency-dependent antenna characteristics like input impedance are derived through a similar approach discussed in Fig. 6(c).

D. COMPARISON WITH CONVENTIONAL OPTICAL ANTENNAS

As the last point, it may be worth discussing the differences between laser and conventional optical antennas via full-wave simulations. The key difference between a VCTL and an

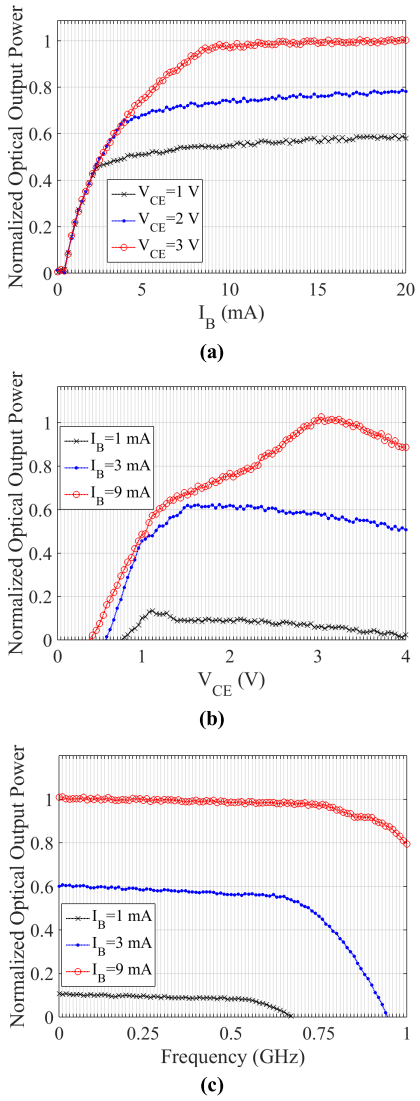

FIGURE 6. Parametric sweep of the base current (I_B) versus different collector-emitter voltages (V_{CE}) in (a) shows the trend of optical output power across the active and threshold regions. Similar trend is demonstrated when sweeping V_{CE} for different values of I_B in (b). In addition to the above DC analyses, small signal analysis of optical response is given in (c).

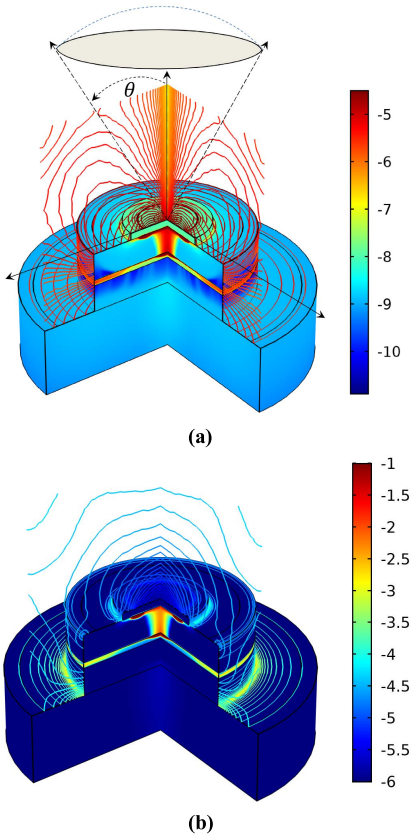

FIGURE 7. VCTL can operate as a conventional optical antenna if only spontaneous emission is considered. (a) Emission rate (log) (W/m^3) and the contour of magnetic power. (b) Electron concentration (log) ($1/m^3$) and the contour of electric power.

optical antenna is described by the stimulated radiative term R_{rad}^{stim}, included in the light-emitting process of laser antennas in (5). Hence, no further development from (7) to (20) is required when dealing with light-emitting semiconductors as conventional optical antennas. Fig. 7 demonstrates the aforementioned difference by excluding R_{rad}^{stim} from calculations. The emission rate and electron concentration are similar to Fig. 4, as the contribution of R_{rad}^{stim} in the above quantities is several orders of magnitude lower than R_{rad}^{spon} [1]. As seen, the spontaneous emission of light from the cavity of laser is similar to a usual cavity antenna having a main beam and some minor sidelobes. The above difference is translated into antenna engineering when calculating the directivity of optical and laser antennas. As shown in Fig. 4, the stimulated emission propagates alongside a straight line leading to pencil-beam directivity. The purpose of this comparison is to highlight a basic difference between the radiation pattern of conventional optical antennas and laser ones. As such, we may not concern ourselves with very minor beam-widening effects happening in lasers, or the presence of minor sidelobes in conventional optical antennas.

The following definition of directivity, as a sufficient measure to provide a basic comparison, is thus implemented. If the solid angle of the main beam (assumed to be the only beam in laser) is defined as Θ, the following approximation for directivity is valid [37],

$$D \approx \frac{4\pi}{\Theta} \tag{26}$$

where the solid angle of the main beam can be conically calculated as $\Theta = 2\pi(1 - \cos\theta)$, with θ as the elevation angle in spherical coordinates asymptotic to the main beam shown in Fig. 7.

For conventional optical antenna in Fig. 7, $\theta \approx 0.2$ (rad) at far-field resulting in $D \approx 20$ dB. Apparently, the calculated directivity is independent of the surface size of the upper mirror. For laser antennas in Fig. 4, where the size of the upper mirror determines Θ, the nanoscale VCTL in Fig. 1 has

$\theta \approx 10^{-7}$ (diameter of the upper mirror is $\sim 10^{-7}$), resulting in an ultra-high directivity $D \approx 235.8$ dB. Even if VCTL is designed in micro or millimeter scales, the spherical angles are $\theta \approx 10^{-4}$ and $\theta \approx 10^{-1}$ respectively, which still lead to extremely high directivities $D \approx 157.2$ dB and $D \approx 78.6$ dB. The values can be verified by the very narrow 3-dB far-field beamwidth of VCTL in [1].

Nevertheless, the above ultra-high directivity cannot lead to a remarkable gain G, because the optical and stimulated efficiencies involved in the light-emitting process of semiconductors are very low. An extremely small portion of radiation is usually attributed to the stimulated emission with efficiency $exp(-\frac{\hbar\omega_0}{K_B T})$. In addition, the efficiency of every laser in converting the input electric power into any type of radiation (either spontaneous or stimulated) is very low too, generically taken around a few percent (say 5%). Therefore, the multiplication of both efficiencies as $0.05e^{-\frac{\hbar\omega_0}{K_B T}}$ leads to a low gain,

$$\mathrm{G} \approx (\mathrm{D} - 371)\ \mathrm{dB} \tag{27}$$

In room temperature. For conventional optical antennas, the coefficient $exp(-\frac{\hbar\omega_0}{K_B T})$ is dropped from gain calculations resulting in a much higher gain (say G $\approx$ (D-13) dB for Fig. 7). We note, however, that the advantage of laser antennas is not to provide a high gain. Instead, they possess very wide bandwidth and highly secured point-to-point communication desired in many modern applications like satellite communications for high data rate transfer [38] or high-precision Earth gravity measurements [39].

IV. CONCLUSION

An accurate physical model for VCTL, capable of incorporating the electromagnetic features of light like polarization, propagation pattern, bandwidth, directivity, gain, and power flow was presented. The model introduces a paradigm for implementing the device as an antenna or rectenna. The equations involve the DC model of semiconductors, which initiates a recombination process, and an eigenvalue problem standing for the interacting photons. Coupling these steps and solving the nonlinear equations by FEM-based solvers will lead to the determination of electromagnetic features of VCTL in emission and absorption modes. The proposed electromagnetic model is in general agreement with experimental reports in both DC and small signal analyses.

APPENDIX
CONVENTIONAL ELECTROMAGNETIC MODEL OF SEMICONDUCTOR LASERS

The motivation of this article is to propose a precise electromagnetic model for VCTL implementable in antenna and rectenna applications. It is thus worth discussing how the polarization and propagation of light is usually considered in the current semiconductor modeling.

In the current models, the wave number vector of photons in an arbitrary direction is defined as,

$$\vec{\boldsymbol{k}} = k\sin\theta\cos\varphi\hat{a}_x + k\sin\theta\sin\varphi\hat{a}_y + k\cos\theta\hat{a}_z \tag{A1}$$

Let us now consider a vertical polarization case where the direction of oscillation of the photon, as an electromagnetic wave, is $\hat{a}_x$,

$$\vec{\boldsymbol{A}} = A_x\hat{a}_x \tag{A2}$$

The average matrix element of the corresponding semiconductor is derived as [28],

$$\mathrm{I}^2 = \frac{-\omega_0^2}{4\pi}\int_0^{\pi}\sin\theta d\theta \times \int_0^{2\pi}\left(\cos^2\theta\cos^2\varphi + \sin^2\varphi\right)\left|A_x\hat{a}_x \times \vec{\nabla} \times A_x\hat{a}_x\right|^2 d\varphi \tag{A3}$$

In current models, the description of photon in (A2) is assumed as a plane wave,

$$\vec{\boldsymbol{A}} = A_0 e^{-j\vec{\boldsymbol{k}}\cdot\vec{\boldsymbol{r}}}\hat{a}_x \tag{A4}$$

wherein no geometrical features of the device, like those in (11) with precise boundary conditions, are incorporated. As such, the average matrix element is approximated as,

$$\mathrm{I}^2 = \frac{A_0^4}{3}\left|\hat{a}_x \times \vec{\nabla} \times e^{-j\vec{\boldsymbol{k}}\cdot\vec{\boldsymbol{r}}}\hat{a}_x\right|^2 \tag{A5}$$

Similar conclusions are valid for horizontal or any other polarization. Detailed discussions on the above equations and their derivations are available in Section 9.5 of [28]. In this article, a systematic reorganization and coupling of the governing equations of VCTL is presented. The magnetic vector potential and classical fields derived in this article are calculated by full-wave computational electromagnetic models to achieve a geometrical description for the device suitable for antenna and rectenna applications..

REFERENCES

[1] H. W. Then, M. Feng, and N. Holonyak, "The transistor laser: Theory and experiment," *Proc. IEEE*, vol. 101, no. 10, pp. 2271–2298, Oct. 2013.

[2] J. Li and N. Engheta, "Core-shell nanowire optical antennas fed by slab waveguides," *IEEE Trans. Antennas Propag.*, vol. 55, no. 11, pp. 3018–3026, Nov. 2007.

[3] M. Agio and A. Alù, *Optical Antennas*. New York, NY, USA: Cambridge Univ. Press, 2013.

[4] F. Monticone, C. Argyropoulos, and A. Alu, "Optical antennas: Controlling electromagnetic scattering, radiation, and emission at the nanoscale," *IEEE Antennas Propag. Mag.*, vol. 59, no. 6, pp. 43–61, Dec. 2017.

[5] M. M. Salary and H. Mosallaei, "Time-modulated conducting oxide metasurfaces for adaptive multiple access optical communication," *IEEE Trans. Antennas Propag.*, vol. 68, no. 3, pp. 1628–1642, Mar. 2020.

[6] C. Tsokos, E. Andrianopoulos, A. Raptakis, N. Lyras, L. Gounaridis, P. Groumas, R. B. Timens, I. Visscher, R. Grootjans, L. S. Wefers, D. Geskus, E. Klein, H. Avramopoulos, R. Heideman, C. Kouloumentas, and C. Roeloffzen, "True time delay optical beamforming network based on hybrid InP-silicon nitride integration," *J. Lightw. Technol.*, vol. 39, no. 18, pp. 5845–5854, Sep. 15, 2021.

[7] C.-S. Im, S.-M. Kim, K.-P. Lee, S.-H. Ju, J.-H. Hong, S.-W. Yoon, T. Kim, E.-S. Lee, B. Bhandari, C. Zhou, S.-Y. Ko, Y.-H. Kim, M.-C. Oh, and S.-S. Lee, "Hybrid integrated silicon nitride–polymer optical phased array for efficient light detection and ranging," *J. Lightw. Technol.*, vol. 39, no. 13, pp. 4402–4409, Jul. 1, 2021.
[8] M. Camacho, A. Nekovic, S. Freer, P. Penchev, R. R. Boix, S. Dimov, and M. Navarro-Cia, "Symmetry and finite-size effects in quasi-optical extraordinarily THz transmitting arrays of tilted slots," *IEEE Trans. Antennas Propag.*, vol. 68, no. 8, pp. 6109–6117, Aug. 2020.
[9] L. Dussopt, K. Medrar, and L. Marnat, "Millimeter-wave Gaussian-beam transmitarray antennas for quasi-optical *S*-parameter characterization," *IEEE Trans. Antennas Propag.*, vol. 68, no. 2, pp. 850–858, Feb. 2020.
[10] E. Dakar, E. Golbraikh, N. S. Kopeika, and A. Zilberman, "Effect of the zenith angle on optical wave propagation in anisotropic non-Kolmogorov atmospheric turbulence: A new experiment-based model," *IEEE Trans. Antennas Propag.*, vol. 68, no. 8, pp. 6287–6295, Aug. 2020.
[11] G. Moddel and S. Grover, *Rectenna Solar Cells*. New York, NY, USA: Springer, 2013.
[12] T. J. Brockett, H. Rajagopalan, R. B. Laghumavarapu, D. Hufakker, and Y. Rahmat-Samii, "Electromagnetic characterization of high absorption sub-wavelength optical nanostructure photovoltaics for solar energy harvesting," *IEEE Trans. Antennas Propag.*, vol. 61, no. 4, pp. 1518–1527, Apr. 2013.
[13] C. Bahhar, C. Baccouche, and H. Sakli, "Optical RECTENNA for energy harvesting and RF transmission in connected vehicles," in *Proc. 17th Int. Multi-Conf. Syst., Signals Devices (SSD)*, Jul. 2020, pp. 262–266.
[14] D. Yadav, "Solar energy harvesting by carbon nanotube optical rectenna: A review," in *Proc. IEEE Int. Symp. Sustain. Energy, Signal Process. Cyber Secur. (iSSSC)*, Dec. 2020, pp. 1–5.
[15] S. Joshi and G. Moddel, "Simple figure of merit for diodes in optical rectennas," *IEEE J. Photovolt.*, vol. 6, no. 3, pp. 668–672, May 2016.
[16] Z. Zhu, S. Grover, K. Krueger, and G. Moddel, "Optical rectenna solar cells using graphene geometric diodes," in *Proc. 37th IEEE Photovoltaic Spec. Conf.*, Jun. 2011, pp. 2120–2122.
[17] R. H. Hadfield, "Single-photon detectors for optical quantum information applications," *Nature Photon.*, vol. 3, pp. 696–705, Dec. 2009.
[18] C. Di Garbo, P. Livreri, and G. Vitale, "Optimal matching between optical rectennas and harvester circuits," in *Proc. IEEE Int. Conf. Environ. Electr. Eng. IEEE Ind. Commercial Power Syst. Eur.*, Jun. 2017, pp. 1–6.
[19] E. H. Shah, B. Brown, and B. A. Cola, "A study of electrical resistance in carbon nanotube–insulator–metal diode arrays for optical rectenna," *IEEE Trans. Nanotechnol.*, vol. 16, no. 2, pp. 230–238, Mar. 2017.
[20] B. Khayatian and Y. Rahmat-Samii, "A novel antenna concept for future solar sails: Application of Fresnel antennas," *IEEE Antennas Propag. Mag.*, vol. 46, no. 2, pp. 50–63, Apr. 2004.
[21] K. Achouri, O. V. Cespedes, and C. Caloz, "Solar 'meta-sails' for agile optical force control," *IEEE Trans. Antennas Propag.*, vol. 67, no. 11, pp. 6924–6934, Nov. 2019.
[22] Q. L. Zhang, B. J. Chen, K. F. Chan, and C. H. Chan, "Terahertz circularly- and linearly polarized leaky-wave antennas based on spin–orbit interaction of spoof surface plasmon polaritons," *IEEE Trans. Antennas Propag.*, vol. 69, no. 8, pp. 4347–4358, Aug. 2021.
[23] G. Slepyan, T. Gilad, and A. Boag, "Quantum light rectification in nano-rectennas," in *Proc. IEEE Int. Symp. Antennas Propag. USNC/URSI Nat. Radio Sci. Meeting*, Jul. 2017, pp. 1051–1052.
[24] A. M. A. Sabaawi, C. C. Tsimenidis, and B. S. Sharif, "Characterization of coupling and quantum efficiencies in solar rectennas," in *Proc. Loughborough Antennas Propag. Conf. (LAPC)*, Nov. 2013, pp. 363–368.
[25] S. Selberherr, *Analysis and Simulation of Semiconductor Devices*. Wien, Austria: Springer, 1984.
[26] S. S. Li, *Semiconductor Physical Electronics*, 2nd ed. New York, NY, USA: Springer, 2006.
[27] A. Yariv, *Quantum Electronics*. Hoboken, NJ, USA: Wiley, 1989.
[28] S. L. Chuang, *Physics of Photonic Devices*. Hoboken, NJ, USA: Wiley, 2009.
[29] W. C. Chew, A. Y. Liu, C. Salazar-Lazaro, and W. E. I. Sha, "Quantum electromagnetics: A new look—Part I," *IEEE J. Multiscale Multiphys. Comput. Techn.*, vol. 1, pp. 73–84, 2016.
[30] W. C. Chew, A. Y. Liu, C. Salazar-Lazaro, and W. E. I. Sha, "Quantum electromagnetics: A new look—Part II," *IEEE J. Multiscale Multiphys. Comput. Techn.*, vol. 1, pp. 73–84, 2016.
[31] A. Afsari, A. Heidari, and M. Movahhedi, "3D meshless simulation of laser ray deviation under thermal lensing effect," *Int. J. Numer. Model., Electron. Netw., Devices Fields*, vol. 29, no. 3, pp. 407–416, May 2016.
[32] J. Jackson, *Classical Electrodynamics*, 3rd ed. New York, NY, USA: Wiely, 1999.
[33] A. Afsari, A. Abbosh, and Y. Rahmat-Samii, "Re-expressing the solution of Maxwell equations using two new auxiliary scalar potentials," in *Proc. IEEE Int. Symp. Antennas Propag. USNC/URSI Nat. Radio Sci. Meeting*, San Diego, CA, USA, Jul. 2017, pp. 33–34.
[34] W. Shi, L. Chrostowski, and B. Faraji, "Numerical study of the optical saturation and voltage control of a transistor vertical-cavity surface-emitting laser," *IEEE Photon. Technol. Lett.*, vol. 20, no. 24, pp. 2141–2143, Dec. 15, 2008.
[35] A. E. Bulyshev, A. E. Souvorov, S. Y. Semenov, V. G. Posukh, and Y. E. Sizov, "Three-dimensional vector microwave tomography: Theory and computational experiments," *Inverse Problems*, vol. 20, no. 4, pp. 1239–1259, Jun. 2004.
[36] A. Afsari, A. M. Abbosh, and Y. Rahmat-Samii, "Adaptive beamforming by compact arrays using evolutionary optimization of Schelkunoff polynomials," *IEEE Trans. Antennas Propag.*, vol. 70, no. 6, pp. 4485–4497, Jun. 2022, doi: 10.1109/TAP.2022.3140347.
[37] C. A. Balanis, *Antenna Theory: Analysis and Design*, 4th ed. Hoboken, NJ, USA: Wiley, 2016.
[38] *Laser Communications Relay Demonstration (LCRD)*. Accessed: Jun. 29, 2022. [Online]. Available: https://www.nasa.gov/mission_pages/tdm/lcrd/index.html
[39] *Gravity Recovery and Climate Experiment (GRACE)*. Accessed: Jun. 27, 2022. [Online]. Available: https://www.jpl.nasa.gov/news/prolific-earth-gravity-satellites-end-science-mission

ARMAN AFSARI (Member, IEEE) received the Ph.D. degree in electrical engineering from The University of Queensland, Brisbane, QLD, Australia, in 2019.

He was a Postdoctoral Research Fellow with the School of Information Technology and Electrical Engineering, The University of Queensland. He is currently a Research Fellow with the School of Information and Communication Technology, Griffith University, Australia, where he conducts research on satellite sensors for cosmic radiation measurement. His research interests include computational electromagnetics, inverse scattering, and radar beamforming. He was a recipient of several IEEE conference awards, The University of Queensland most appropriate Ph.D. candidate award, and the IEEE TRANSACTIONS ON ANTENNAS AND PROPAGATION outstanding reviewer award.

PAULO DE SOUZA (Senior Member, IEEE) received the Ph.D. degree in natural sciences from the Johannes Gutenberg University of Mainz, Rhineland-Palatinate, Germany, in 2004.

He was the Chief Research Scientist with the Commonwealth Scientific and Industrial Research Organisation (CSIRO), Australia. He is currently a Professor, the Dean of the Research for Sciences Group, and the Former Head of the School of Information and Communication Technology, Griffith University, Australia. He has authored or coauthored more than 200 technical journal and conference papers, book chapters, and is the holder of many patents. He is a fellow of the Australian Computer Society. He serves as an editorial board member of several interdisciplinary journals. He is a reviewer of several research funding programs across the world. He has extensive international hands-on experience in industrial research, consultancy, government agencies, and academia.

AMIN ABBOSH (Fellow, IEEE) received the Doctor of Engineering degree from The University of Queensland, Brisbane, QLD, Australia, in 2013. He is currently a Professor, the Leader of the Electromagnetic Innovations (EMAGIN) Group, and the Former Head of the School of Information Technology and Electrical Engineering, The University of Queensland. He has authored or coauthored more than 400 articles on electromagnetic imaging systems, wideband passive microwave devices, and planar antennas. He is a two-time winner of the IEEE AP-S King Prize for the best paper published in the IEEE TRANSACTIONS ON ANTENNAS AND PROPAGATION.

YAHYA RAHMAT-SAMII (Life Fellow, IEEE) received the Ph.D. degree in electrical engineering from the University of Illinois at Urbana–Champaign, Champaign, IL, USA, in 1975. He was a Senior Research Scientist with the Caltech/NASA's Jet Propulsion Laboratory. He is currently a Distinguished Professor, the Holder of the Northrop-Grumman Chair in electromagnetics, a member of the U.S. National Academy of Engineering (NAE), a Foreign Member of the Chinese Academy of Engineering (CAE) and the Royal Flemish Academy of Belgium for Science and the Arts, the winner of the 2011 IEEE Electromagnetics Field Award, and the Former Chairperson of the Electrical Engineering Department, University of California at Los Angeles (UCLA), Los Angeles, CA, USA. He has authored or coauthored more than 1100 technical journal and conference papers, written over 36 book chapters and six books, and is the holder of many patents. He has more than 20 cover-page IEEE publication articles.

He is a fellow of AMTA, ACES, EMA, and URSI. He was a recipient of the Henry Booker Award from URSI, in 1984, which is given triennially to the most outstanding young radio scientist in North America, the Best Application Paper Prize Award (Wheeler Award) of the IEEE TRANSACTIONS ON ANTENNAS AND PROPAGATION, in 1992 and 1995, the University of Illinois ECE Distinguished Alumni Award, in 1999, and the IEEE Third Millennium Medal and the AMTA Distinguished Achievement Award, in 2000. In 2001, he received an Honorary Doctorate Causa from the University of Santiago de Compostela, Spain. He received the 2002 Technical Excellence Award from JPL, the 2005 URSI Booker Gold Medal presented at the URSI General Assembly, the 2007 IEEE Chen- To Tai Distinguished Educator Award, the 2009 Distinguished Achievement Award of the IEEE Antennas and Propagation Society, the 2010 UCLA School of Engineering Lockheed Martin Excellence in Teaching Award, and the 2011 campus-wide UCLA Distinguished Teaching Award. He was also a recipient of the Distinguished Engineering Educator Award from The Engineers Council in 2015, the John Kraus Antenna Award of the IEEE Antennas and Propagation Society and the NASA Group Achievement Award, in 2016, the ACES Computational Electromagnetics Award, and the IEEE Antennas and Propagation S. A. Schelkunoff Best Transactions Prize Paper Award, in 2017. He was a recipient of the prestigious Ellis Island Medal of Honor, in 2019. The medals are awarded annually to an exceptionally small group of distinguished U.S. citizens who exemplify a life dedicated to community service. These are individuals who preserve and celebrate the history, traditions, and values of their ancestry while exemplifying the values of the American way of life and are dedicated to creating a better world. Among the recipients of this honor are seven former presidents of the United States of America, to name a few. He is listed in Who's Who in America, Who's Who in Frontiers of Science and Technology, and Who's Who in Engineering. He has been a plenary and a millennium session speaker at numerous national and international symposia. He has been the organizer and the presenter of many successful short courses worldwide. Many of his students have won major theses and conference paper awards. He has had pioneering research contributions in diverse areas of electromagnetics, antennas, measurements and diagnostics techniques, numerical and asymptotic methods, satellite and personal communications, human/antenna interactions, RFID and implanted antennas in medical applications, frequency-selective surfaces, electromagnetic band-gap and meta-material structures, applications of the genetic algorithms, and particle swarm optimizations. He is the Designer of the IEEE Antennas and Propagation Society logo, displayed on all the official correspondence of the IEEE Antennas and Propagation Society. He was the President of the IEEE Antennas and Propagation Society, in 1995, and the President of the United States National Committee (USNC) of the International Union of Radio Science (URSI), from 2009 and 2011. He has also served as an IEEE Distinguished Lecturer presenting lectures internationally.